NANO LETTERS

Open Access
This article is licensed under CC-BY-NC-ND 4.0

pubs.acs.org/NanoLett
Letter

Volatile and Nonvolatile Resistive Switching in Lateral 2D Molybdenum Disulfide-Based Memristive Devices

Sofía Cruces, Mohit D. Ganeriwala, Jimin Lee, Ke Ran, Janghyun Jo, Lukas Völkel, Dennis Braun, Bárbara Canto, Enrique G. Marín, Holger Kalisch, Michael Heuken, Andrei Vescan, Rafal E. Dunin-Borkowski, Joachim Mayer, Andrés Godoy, Alwin Daus, and Max C. Lemme*

Cite This: *Nano Lett.* 2025, 25, 12455−12462

Read Online

ACCESS | Metrics & More | Article Recommendations | Supporting Information

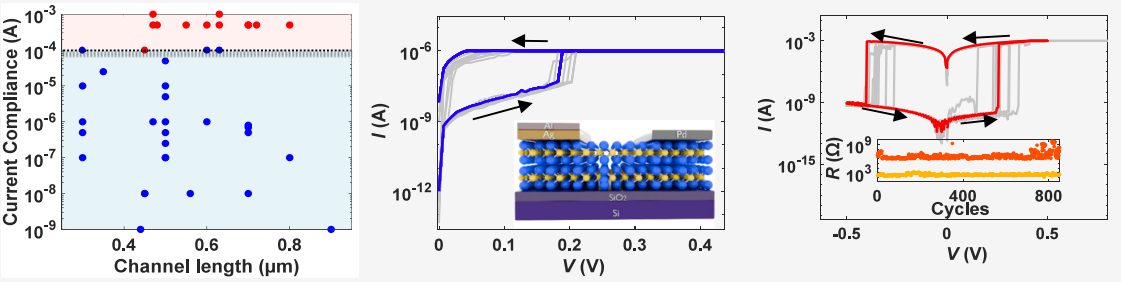

ABSTRACT: Developing electronic devices capable of emulating biological functions is essential for advancing brain-inspired computation paradigms such as neuromorphic computing. In recent years, two-dimensional materials have emerged as promising candidates for neuromorphic electronic devices. This work addresses the coexistence of volatile and nonvolatile resistive switching in lateral memristors based on molybdenum disulfide with silver as the active electrode. The fabricated devices exhibited switching voltages of ∼0.16 V and ∼0.52 V for volatile and nonvolatile operation, respectively, under direct-current measurements. They also displayed the essential synaptic functions of paired-pulse facilitation and short- and long-term plasticity under pulse stimulation. The operation mechanism was investigated by *in situ* transmission electron microscopy, which showed lateral migration of silver ions along the molybdenum disulfide between electrodes. Based on the experimental data, a macroscopic semiclassical electron transport model was used to reproduce the current−voltage characteristics and support the proposed underlying switching mechanisms.

KEYWORDS: *lateral memristor, ion migration, molybdenum disulfide, resistive switching, volatile, nonvolatile*

Downloaded via RWTH AACHEN HOCHSCHUL BIBL on August 25, 2025 at 12:58:16 (UTC).
See https://pubs.acs.org/sharingguidelines for options on how to legitimately share published articles.

Emulating the brain and its biological functions with circuits based on conventional complementary metal-oxide semiconductor (CMOS) technology requires complex circuitry, which leads to high energy consumption.[1,2] In this scenario, resistive switching (RS) devices are promising candidates for implementing the desired artificial neurons and multifunctional synaptic devices in neuromorphic hardware. Among the wide variety of RS devices, electrochemical metallization (ECM) memristors based on two-dimensional (2D) materials exhibit particularly promising features as vertical and lateral memristors.[3−5] ECM memristors are characterized by the formation and rupture of metallic conductive filaments (CFs) under an applied electrical field.[6−8] These CFs usually originate from the migration of active metal ions such as silver (Ag) or copper (Cu).[9] Up to date, CFs composed of Ag ions have been visualized in several device architectures.[3,10−13] ECM memristive devices based on layered 2D materials (2DMs), including molybdenum disulfide (MoS_2), have demonstrated low energy consumption of approximately 10 fJ, low switching voltages of <0.3 V, and RS in subnanometer thicknesses.[3,14−19] However, the growth and evolution of metallic CFs in 2DM ECM memristors rely on random defects,[10] which often lead to high cycle-to-cycle and device-to-device variability.

Lateral 2DM-based devices, in which 2DMs are placed on a dielectric substrate and contacted by metal electrodes, have been extensively studied as RS devices.[3,11,20−27] Lateral memristive devices present three key benefits over conventional vertical stacks: (i) the selector functionality can be easily integrated; (ii) they enable simultaneous signal transmission and learning; and (iii) they support spatiotemporal information processing.[26,28] However, the switching mechanisms in lateral devices for volatile and nonvolatile operation (and their coexistence) remain largely unexplored. In fact, the coexistence

Received: April 2, 2025
Revised: July 10, 2025
Accepted: July 10, 2025
Published: August 7, 2025

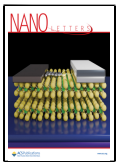

ACS Publications
© 2025 The Authors. Published by American Chemical Society

https://doi.org/10.1021/acs.nanolett.5c01992
Nano Lett. 2025, 25, 12455−12462

of both RS modes by tuning the measurement system's current compliance (CC) has been only shown for vertical devices based on metal oxides and hexagonal boron nitride.[29−34] The coexistence of both RS modes within a single device could enhance the implementation of both synaptic devices and artificial neurons for future neuromorphic systems.

Here, we investigate the coexistence of volatile and nonvolatile RS in lateral MoS_2-based memristors using Ag as the filament-forming electrode. We show the transition between volatile and nonvolatile switching modes by tuning the CC of direct-current (DC) electrical measurements. Furthermore, we demonstrate the coexistence of both modes under pulsed voltage stress (PVS). We also show short-term (STP) and long-term plasticity (LTP) in response to different pulsed stimulation and analyze the RS mechanisms for both volatile and nonvolatile switching modes. The growth and stability of the CFs depend on several factors, such as the filament morphology and the applied electrical field.[9,10,35] Therefore, we conducted *in situ* transmission electron microscopy (TEM) images to analyze Ag migration along the MoS_2. Finally, we applied a semiclassical electron transport model that reproduces the experimental current−voltage (*I-V*) characteristics and supports the formation of metallic Ag CFs as the switching mechanism.

Our lateral devices comprise multilayer MoS_2 contacted by palladium (Pd) and active Ag electrodes with a submicron channel length (see schematic in Figure 1a). First, MoS_2 grown

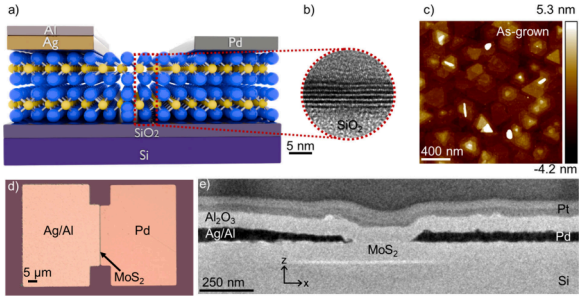

Figure 1. Device structure and material characterization. (a) Cross-sectional schematic of the lateral MoS_2-based memristor. (b) HRTEM image of the multilayer MoS_2 film between the metal electrodes. (c) AFM image of the as-grown MoS_2 on sapphire. (d) Top-view optical microscopy image of a fabricated lateral device. (e) TEM image showing the cross section of a device. The channel length was approximately 250 nm. Al_2O_3 was e-beam-evaporated to protect the MoS_2 during FIB.

by metal−organic chemical vapor deposition (MOCVD) on a 2" sapphire wafer was wet transferred onto a SiO_2/Si substrate.[36] The Pd electrodes were defined using optical lithography, and the Ag ones were defined using a laser writer. The Ag electrodes were covered *in situ* with a 50 nm aluminum (Al) electron-beam-evaporated (e-beam) capping layer to avoid tarnishing.[21] Reactive ion etching (RIE) was carried out to pattern the MoS_2 channels. More details about the device fabrication are available in the Materials and Methods section in the Supporting Information (SI), and a schematic process flow with each step is displayed in Supplementary Figure S1.

The devices were characterized by high-resolution TEM (HRTEM). The layered structure of the MoS_2 in a device in Figure 1b shows an interlayer distance of 6.4 ± 0.05 Å, in line with values reported in the literature.[37,38] The atomic force microscopy (AFM) image in Figure 1c reveals a polycrystalline nature of the as-grown MoS_2 on 2" sapphire. Additional AFM confirms the thickness of ∼4.4 nm of the MoS_2 film (Supplementary Figure S2a). In addition, we conducted Raman spectroscopy measurements of the as-grown MoS_2 on sapphire and after transfer on SiO_2/Si. The extracted E^1_{2g} and A_{1g} peaks of MoS_2 coincide with the literature values for more than four layers or the bulk, which is in agreement with the AFM and HRTEM data (see Figure S2b).[39,40] Furthermore, the photoluminescence peak position of 1.82 eV corroborates the multilayered nature of the MoS_2 and the good crystal quality of the transferred material (Figure S2c-d).[41−43] Figure 1d shows a top-view optical microscopy image of a fabricated device. A lamella was cut from a device by focused ion beam (FIB) milling, and a cross-sectional TEM image was taken to verify the integrity of the lamella. The channel length between the metal electrodes was ∼250 nm in this specific device. For the *in situ* TEM measurements, the channels of the devices were covered with an additional 80 nm e-beam-evaporated aluminum oxide (Al_2O_3) film to protect the MoS_2 from the ion beam during the FIB lamella preparation. Moreover, the Al_2O_3 layer prevents direct contact between the platinum (Pt) protection layer used in FIB and both the electrodes and MoS_2 layers, which would otherwise lead to a short circuit.

We conducted DC electrical measurements on the Pd/MoS_2/Ag/Al devices with CC values varying from 100 nA to 1 mA. More information regarding the influence of the CC values and the devices' behavior can be seen in Figure S3. Volatile RS was observed for CC values from 100 nA up to 100 μA (Figure 2a). Figure 2b shows ten *I-V* curves with a 1 μA CC measured in subsequent voltage sweeps in the positive polarity and plotted in logarithmic scale (see linear scale in SI Figure S4a). The first sweep is marked in blue. We attribute the forming-free nature of our device to the submicron channel length which can promote filament formation at lower voltages.[21] The voltage bias was applied to the Ag active electrode, while the Pd electrode was grounded. The arrows indicate the voltage sweep direction. Initially, the device was in a high-resistance state (HRS) until the SET transition occurred at an on-threshold voltage of $V_{t,on}$ = 0.19 V, when it switched to its low-resistance state (LRS). During the backward sweep, the device switched back to the HRS at a hold voltage of V_{hold} = 0.087 V. We plotted $V_{t,on}$ and V_{hold} in histograms, and the data were fitted with Gaussian distributions that show reasonably low standard deviations (σ) of 0.04 and 0.03 V, respectively (Figure S5). The mean $V_{t,on}$ of 0.16 V is the lowest reported among similar lateral MoS_2-based RS devices (see Table 1).[11,12,21,22,24] In addition to the table, Figure S6 presents the key benchmarking values including the material, channel length and $V_{t,on}$ in a concise graph. Figure 2c shows the normalized cumulative distribution functions (CDFs) of $V_{t,on}$ and V_{hold} for 60 consecutive volatile cycles, with a standard error of 3.9% and 3.1%, respectively (see Figure S4b for the corresponding *I-V* curves). Furthermore, Figure S7a shows the behavior of $V_{t,on}$ for 5 devices with different channel lengths. The $V_{t,on}$ decreases with decreasing channel lengths which is in good agreement with the literature.[12,21,22]

Nonvolatile bipolar RS was observed for CC values above 100 μA (Figure 2d). We then performed ten consecutive *I-V* sweeps with 1 mA CC, with the first sweep marked in red (Figure 2e). The extracted mean SET and RESET voltages of these switching cycles were V_{SET} = 0.26 V and V_{RESET} = −0.36 V. The inset in Figure 2e shows the DC endurance of a single device for ∼860 consecutive nonvolatile RS cycles with an

https://doi.org/10.1021/acs.nanolett.5c01992
Nano Lett. 2025, 25, 12455−12462

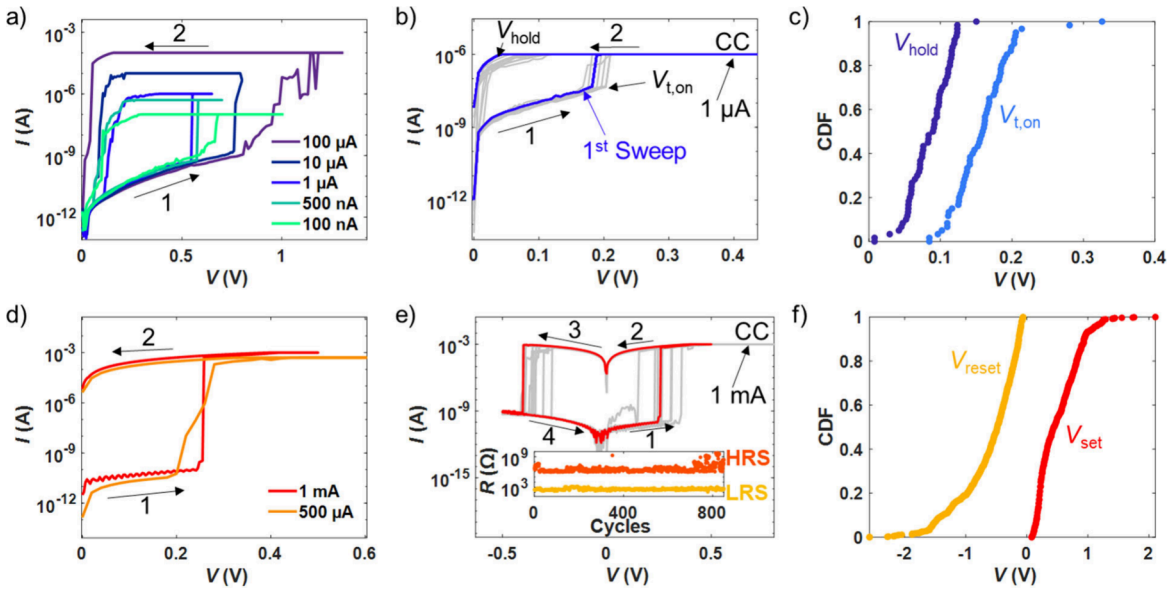

Figure 2. DC electrical performance of the lateral MoS_2-based devices. (a) Volatile RS at different CC values from 100 nA up to 100 μA. (b) 10 subsequent volatile switching curves recorded with positive voltage polarity for 1 μA CC. The arrows indicate the voltage sweeping directions, with the first sweep marked in blue. (c) CDFs of the $V_{t,on}$ and the V_{hold} of 60 consecutive volatile $I-V$ curves. (d) Nonvolatile RS at 500 μA and 1 mA CC. (e) 10 consecutive nonvolatile I-V curves for 1 mA CC. The inset shows the resistance values for ~860 nonvolatile consecutive cycles. (f) CDFs of the V_{SET} and V_{RESET} of ~860 nonvolatile cycles.

Table 1. Comparison of Our Work with Other Similar 2D-Based Literature

ref.	Device structure	Material	Thickness and Channel length	Forming voltage (V)	Volatile ($V_{t,on}$)	Nonvolatile (V_{SET})	*In situ* switching mechanism
This work	**Lateral**	**MOCVD-grown MoS_2**	**4.4 nm 250−900 nm**	**Forming-free**	**O (0.16 V)**	**O (0.52 V)**	**O**
24	Lateral	CVD-grown MoS_2	Monolayer 2 μm	~20 V	–	O (3.5−8.3 V)	O
3	Lateral	CVD-grown MoS_2	Monolayer 500 nm	~4 V	O (1.2 V)	–	O
22	Lateral	Mechanically exfoliated MoS_2	<6 layers 18 nm	1.8 V	O (0.35 V)	–	–
12	Lateral	Mechanically exfoliated MoS_2	4−30 layers 250 nm	~3.8 V	–	O (2 V)	O
11	Lateral	CVD-grown MoS_2	Monolayer 5 μm	Forming-free	–	O (10−20 V)	O
10	Lateral	Exfoliated MoS_2 nanoflakes	>1 layer 15 nm	–	–	O (~6 V)	O
52	Vertical	CVD-grown vertically aligned MoS_2	~23 nm 23 nm	Forming-free	O (~0.35 V)	–	–

average HRS-to-LRS resistance ratio (R_{HRS}/R_{LRS}) of more than 10^4. We further measured the retention time of both the HRS and the LRS of a device (Figure S8). The device remained in the LRS for at least 8 days and in the HRS for ~12 h. Furthermore, we measured the retention of 5 different LRS states for at least 1000 s (Figure S9). Figure 2f displays the corresponding cumulative voltage distributions with a mean V_{SET} and V_{RESET} of ~0.52 V and ~−0.61 V, and standard deviations of σ = 0.3 V and σ = 0.4 V, respectively. Figure S10 shows the CDFs of V_{set} and V_{reset} for 4 devices with a standard error of 5.07% and 4.4% for V_{SET} and V_{RESET}, respectively. We further demonstrated that not only can we observe volatile and nonvolatile switching but also, we can control the transition between both in the lateral MoS_2 devices solely by modifying the CC value (see Figure S11).

We conducted PVS tests with different pulses to observe the volatile and nonvolatile dynamic responses of our devices. Figure 3a shows the volatile transient current response of a device to a 1 μs voltage pulse of 6 V. The switching time of t_{on} = 250 ns is the time required to reach 90% of the ON current of I_{on} = 12.5 μA. The relaxation time of t_r = 131 ns is defined as the time needed to reach 10% of the difference between I_{on} and the OFF current (I_{off}) when switching back to the HRS.[21] At the end of the voltage pulse, the device spontaneously relaxes to its initial OFF state. Furthermore, we measured the endurance of a device under PVS for over 1060 volatile RS cycles (Figure S12). The on-state resistance (R_{on}) exhibits low cycle-to-cycle variability with a R_{off}/R_{on} ratio of over 12. Figure 3b, in contrast, shows the transient nonvolatile output current response to a 0.02 s voltage pulse of V_{SET} = 3.5 V and a 0.05 s voltage pulse of V_{RESET} = −5 V. Read voltage pulses of V_{read} =

https://doi.org/10.1021/acs.nanolett.5c01992
Nano Lett. 2025, 25, 12455−12462

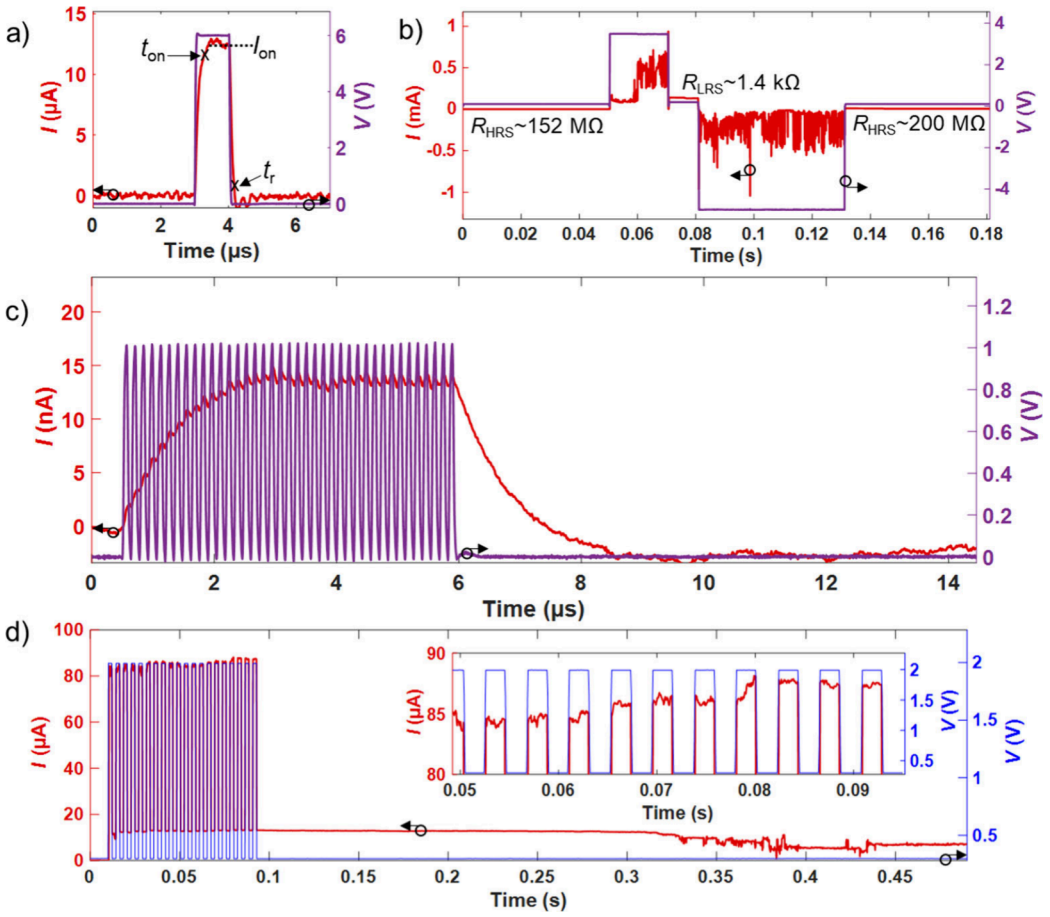

Figure 3. Current response over time of a lateral memristive device upon PVS. (a) Voltage pulse of 6 V for 1 μs showing volatile RS. (b) Nonvolatile RS upon PVS with a 3.5 V/20 ms SET pulse and a −5 V/50 ms RESET pulse. (c) Dynamic response of a device during a sequence of 40 voltage pulses of 1 V for 50 ns showing short-term potentiation with forgetting upon stimuli removal. (d) Train of 20 consecutive 2 V/2 ms pulses showing long-term plasticity. The read voltage applied between each pulse was 0.3 V. The inset shows the gradual increase in the current after each applied pulse.

0.2 and 0.1 V were applied to measure the resistances in the LRS and HRS, respectively. After the SET pulse, the current did not return to its initial OFF-state but remained in the ON-state. The current pulse levels for the nonvolatile switching are over 100 μA, which matches the levels applied in the DC CC-dependent measurements. The R_{LRS} after the SET pulse was ∼1.4 kΩ, whereas the R_{HRS} was ∼200 MΩ.

STP and LTP were investigated by applying a series of consecutive voltage pulses. First, a train of 40 consecutive 1 V/50 ns pulses with a 50 ns period between them was applied and the transient response of our device recorded. The current response in Figure 3c shows a gradual current increase with each pulse, which saturates at 13 nA after about 18 pulses. The current decreases slightly after each pulse and decays to its initial state after the final voltage pulse. The fast relaxation to the initial OFF-state with no memory retention and a relaxation time of t_r = 2.2 μs, emulates STP, i.e., a forgetting process observed in biological synapses.[44] We also achieved LTP in the same device by tuning the programming parameters so the device current increased to a higher value, triggering the nonvolatile regime. Figure 3d shows the device current response to a train of 20 consecutive pulses of an increased voltage of 2 V and a much longer duration of 2 ms. A magnification of the current response in the inset shows a gradual current increase after each applied pulse, resembling the biological synaptic function known as paired-pulse facilitation (PPF). After the final pulse, the current decayed to an intermediate ON-state, in contrast to the previous experiment with 40 smaller, shorter pulses. The retention time of the LRS was recorded for over ∼100 s, more than the time displayed in Figure 3d (see SI Figure S13). This device behavior aligns with the LTP concept, as the LRS lasts for more than a few tens of seconds.[44−46] LTP, long-term depression (LTD) and the increase in postsynaptic conductance (PSC) with varying pulse amplitudes were further investigated. Figure S14 shows the measured synaptic characteristics, specifically the obtained PSC as a function of the number of applied pulses for different amplitudes and polarity configurations. The application of positive pulses (Figure S14a) leads to an increase in PSC, demonstrating LTP. On the contrary, the introduction of a train of negative pulses (Figure S14b) results in a decrease in the PSC, showing Ltd. Figure S14c finally depicts the PSC as a function of the number of pulses for different pulse amplitudes, ranging from 2 V up to 5 V. Controlling the transition from STP to LTP by tuning the programming parameters of the pulse train is in line with previous works on SiO_2 and Ag_2S-based memristors.[45,47]

We further investigated the current conduction mechanisms of our memristive devices. We plotted the $I-V$ curves from Figures 2b (volatile RS) and 2e (nonvolatile) in double-

https://doi.org/10.1021/acs.nanolett.5c01992
Nano Lett. 2025, 25, 12455−12462

logarithmic scale in Figure 4a and Figure 4b, respectively. In the HRS, the *I-V* curves exhibit a square-law dependence,

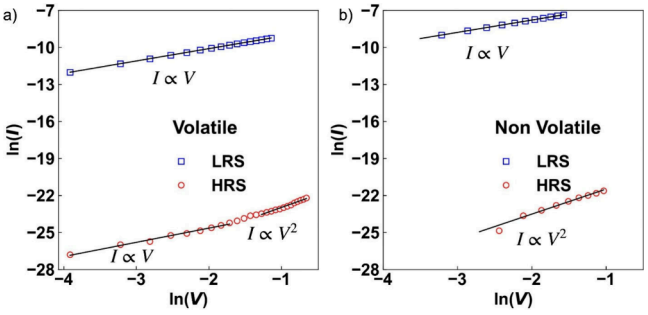

Figure 4. *I-V* characteristics of (a) a volatile and (b) a nonvolatile operation. In both cases, HRS shows SCLC, while LRS shows ohmic transport.

indicating space-charge-limited conduction (SCLC),[48,49] which has been previously reported in two-terminal lateral polycrystalline MoS_2-based devices.[50] In the LRS, the linear *I-V* dependence indicates ohmic conduction. This transition from SCLC in the HRS to ohmic transport in the LRS supports the proposed formation of Ag CFs. Temperature-dependent *I*−*V* measurements confirmed these transport mechanisms (Figure S15). In the HRS, the current increases with increasing temperature, which is characteristic of transport through the MoS_2 channel and SCLC.[50] In the LRS, the current decreases with increasing temperature. Such a negative temperature coefficient of resistivity is characteristic of transport through metallic CFs.[51] Both volatile and nonvolatile RS mechanisms exhibit similar transport characteristics, suggesting the formation of a metallic CF in both cases. However, the applied CC plays a crucial role in determining the RS behavior. We propose that low CC values lead to volatile RS with a weak Ag filament that self-ruptures upon removing the applied voltage. In contrast, higher CC values lead to nonvolatile RS because more Ag ions diffuse into the channel and create a stronger Ag CF. Therefore, we deduce that Ag ions diffuse into the channel driven by the lateral electric field and eventually form continuous Ag filaments. A top-view schematic that illustrates the RS mechanisms for the HRS and the LRS is shown in Figure S16.

We conducted *in situ* TEM on lateral Pd/MoS_2/Ag devices. Figure 5a shows the typical TEM results from a fresh device in the HRS (without any electrical measurement before), including a bright-field TEM image, high-angle annular dark-field (HAADF) images and the corresponding energy-dispersive X-ray spectroscopy (EDXS) elemental maps of Mo, S, and Ag. No traces of Ag are observed between the electrodes within the MoS_2 channel. This observation is confirmed in Figure S17a, where the measured EDXS line profile for Ag is flat across the multilayered MoS_2. The Pd electrode of the device lamella was then electrically biased *in situ* in the TEM while the Ag electrode was grounded (see Figure S17c). The cross-sectional TEM image in Figure 5b shows the lamella device after *in situ* nonvolatile switching to the LRS. The arrows on the TEM image indicate three different regions in which HAADF images and their corresponding EDXS maps were taken (Figure 5c-e). The presence of Ag is clearly visible in these elemental maps. Further, the EDXS line profile of Ag coincides with those of Mo and S, proving the presence of Ag within the MoS_2 channel (Figure S17b). This confirms the formation of an Ag CF following the SET transition. These findings experimentally prove Ag ion migration driven by an applied lateral electrical field, in line with previous reports in the literature.[3,12,22]

We investigated lateral memristive devices with polycrystalline 2D multilayer MoS_2 channels with submicrometer lengths. We demonstrated the coexistence of volatile and nonvolatile RS in the same devices, attainable with both DC and PVS. Our devices display repeatable RS with low switching voltages for both volatile (0.16 V) and nonvolatile (0.52 V) operation. The volatile behavior may be utilized in artificial neurons. We also experimentally demonstrated PPF, STP and LTP behavior in our devices, showcasing their potential as artificial synapses for neuromorphic systems. We investigated the current conduction mechanisms in the HRS and LRS, concluding that SCLC and ohmic transport are the dominant mechanisms, respectively. This behavior can be explained by the formation of Ag conductive filaments, which was confirmed via *in situ* TEM switching experiments. The flexibility of volatile and nonvolatile switching in our lateral memristors can be used to implement both synaptic devices and artificial neurons for future neuromorphic systems.

■ ASSOCIATED CONTENT

Supporting Information

The Supporting Information is available free of charge at https://pubs.acs.org/doi/10.1021/acs.nanolett.5c01992.

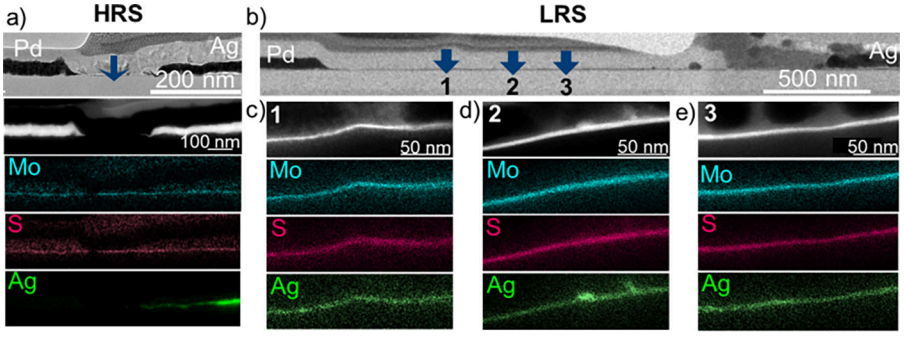

Figure 5. *In situ* TEM measurements for the resistive switching mechanism analysis. (a) Cross-sectional bright-field TEM image, HAADF image and the corresponding EDXS elemental maps of Mo, S, and Ag from a lamella in the HRS before any electrical measurement. The blue arrow denotes the region where the EDXS elemental maps were acquired. (b) Cross-sectional TEM image of a lamella after nonvolatile RS in the LRS. (c−e) EDXS elemental maps of the lamella in the LRS taken on the regions denoted as 1, 2, and 3 in panel b, respectively.

https://doi.org/10.1021/acs.nanolett.5c01992
Nano Lett. 2025, 25, 12455−12462

Materials and methods including MoS_2 growth process, lateral device fabrication, material and device characterization, and electrical measurements; MoS_2 material characterization; schematic of the fabrication process; volatile *I-V* curves in linear and log scale; histogram and Gaussian fit for the on-threshold and hold voltages; transition from volatile to nonvolatile back and forth; LRS retention time; lamella and setup preparation for *in situ* TEM; benchmarking with previous works (PDF)

AUTHOR INFORMATION

Corresponding Author

Max C. Lemme − *Chair of Electronic Devices, RWTH Aachen University, 52074 Aachen, Germany; AMO GmbH, Advanced Microelectronic Center Aachen, 52074 Aachen, Germany;* orcid.org/0000-0003-4552-2411; Email: max.lemme@eld.rwth-aachen.de

Authors

Sofía Cruces − *Chair of Electronic Devices, RWTH Aachen University, 52074 Aachen, Germany;* orcid.org/0000-0003-2816-7016

Mohit D. Ganeriwala − *Department of Electronics and Computer Technology, Facultad de Ciencias, Universidad de Granada, 18071 Granada, Spain;* orcid.org/0000-0003-4682-3435

Jimin Lee − *Chair of Electronic Devices, RWTH Aachen University, 52074 Aachen, Germany;* orcid.org/0000-0002-5877-6958

Ke Ran − *AMO GmbH, Advanced Microelectronic Center Aachen, 52074 Aachen, Germany; Central Facility for Electron Microscopy, RWTH Aachen University, 52074 Aachen, Germany; Ernst Ruska-Centre for Microscopy and Spectroscopy with Electrons (ER-C), Forschungszentrum Jülich GmbH, 52425 Jülich, Germany;* orcid.org/0000-0002-9762-4586

Janghyun Jo − *Ernst Ruska-Centre for Microscopy and Spectroscopy with Electrons (ER-C), Forschungszentrum Jülich GmbH, 52425 Jülich, Germany;* orcid.org/0009-0003-5252-8755

Lukas Völkel − *Chair of Electronic Devices, RWTH Aachen University, 52074 Aachen, Germany;* orcid.org/0000-0002-8138-9980

Dennis Braun − *Chair of Electronic Devices, RWTH Aachen University, 52074 Aachen, Germany;* orcid.org/0000-0003-2803-1784

Bárbara Canto − *AMO GmbH, Advanced Microelectronic Center Aachen, 52074 Aachen, Germany;* orcid.org/0000-0001-5885-9852

Enrique G. Marín − *Department of Electronics and Computer Technology, Facultad de Ciencias, Universidad de Granada, 18071 Granada, Spain*

Holger Kalisch − *Compound Semiconductor Technology, RWTH Aachen University, 52074 Aachen, Germany*

Michael Heuken − *Compound Semiconductor Technology, RWTH Aachen University, 52074 Aachen, Germany; AIXTRON SE, 52134 Herzogenrath, Germany*

Andrei Vescan − *Compound Semiconductor Technology, RWTH Aachen University, 52074 Aachen, Germany;* orcid.org/0000-0001-9465-2621

Rafal E. Dunin-Borkowski − *Ernst Ruska-Centre for Microscopy and Spectroscopy with Electrons (ER-C), Forschungszentrum Jülich GmbH, 52425 Jülich, Germany;* orcid.org/0000-0001-8082-0647

Joachim Mayer − *Central Facility for Electron Microscopy, RWTH Aachen University, 52074 Aachen, Germany; Ernst Ruska-Centre for Microscopy and Spectroscopy with Electrons (ER-C), Forschungszentrum Jülich GmbH, 52425 Jülich, Germany;* orcid.org/0000-0003-3292-5342

Andrés Godoy − *Department of Electronics and Computer Technology, Facultad de Ciencias, Universidad de Granada, 18071 Granada, Spain;* orcid.org/0000-0002-3014-8765

Alwin Daus − *Institute of Semiconductor Engineering, University of Stuttgart, 70569 Stuttgart, Germany;* orcid.org/0000-0001-7461-3756

Complete contact information is available at: https://pubs.acs.org/10.1021/acs.nanolett.5c01992

Author Contributions

M.C.L and A.D. conceived and designed the project. S.C. carried out the material characterization, mask design, device fabrication, and electrical measurements. B.C. supported S.C. with the AFM measurements. H.K, A.V. and M.H. provided the polycrystalline MoS_2. K.R. and J.J. performed *in situ* TEM and EDXS experiments. M.D.G. supported the analysis of the electrical data and the writing. S.C. wrote the initial manuscript, and all authors cowrote it. All authors have given approval to the final version of the manuscript.

Notes

The authors declare no competing financial interest.

ACKNOWLEDGMENTS

Financial support from the German Federal Ministry of Education and Research (BMBF) within the projects NEUROTEC 2 (No. 16ME0399, 16ME0400, and 16ME0403) and the Clusters4Future NeuroSys (No. 03ZU1106AA and 03ZU1106AD) is gratefully acknowledged. We acknowledge funding from the European Union's Horizon Europe research and innovation program (via CHIPS-JU) under the project ENERGIZE (101194458). A.D. acknowledges support by the German Research Foundation through the Emmy Noether Programme (506140715). We also acknowledge support by the Spanish Government through the research projects CNS2023-143727 RECAMBIO, PID2023-150162OB-I00 ADAGE, and TED2021-129769B-I00 FlexPowHar funded by MCIN/AEI/10.13039/501100011033 and the European Union NextGenerationEU/PRTR.

REFERENCES

(1) Park, S.-O.; Jeong, H.; Park, J.; Bae, J.; Choi, S. Experimental Demonstration of Highly Reliable Dynamic Memristor for Artificial Neuron and Neuromorphic Computing. *Nat. Commun.* **2022**, *13* (1), 2888.

(2) Yi, W.; Tsang, K. K.; Lam, S. K.; Bai, X.; Crowell, J. A.; Flores, E. A. Biological Plausibility and Stochasticity in Scalable VO2 Active Memristor Neurons. *Nat. Commun.* **2018**, *9* (1), 4661.

(3) Hao, S.; Ji, X.; Zhong, S.; Pang, K. Y.; Guan Lim, K.; Chong Chong, T.; Zhao, R. A Monolayer Leaky Integrate- and Fire Neuron for 2D Memristive Neuromorphic Networks. *Adv. Electron. Mater.* **2020**, *6* (4), 1901335.

(4) Kalita, H.; Krishnaprasad, A.; Choudhary, N.; Das, S.; Dev, D.; Ding, Y.; Tetard, L.; Chung, H.-S.; Jung, Y.; Roy, T. Artificial Neuron

Using Vertical MoS2/Graphene Threshold Switching Memristors. *Sci. Rep* **2019**, *9* (1), 53.
(5) Mallik, S. K.; Padhan, R.; Sahu, M. C.; Pradhan, G. K.; Sahoo, P. K.; Dash, S. P.; Sahoo, S. Ionotronic WS2Memtransistors for 6-Bit Storage and Neuromorphic Adaptation at High Temperature. *npj 2D Mater. Appl.* **2023**, *7* (1), 63.
(6) Ielmini, D.; Waser, R. *Resistive Switching: From Fundamentals of Nanoionic Redox Processes to Memristive Device Applications*; 2016. DOI: 10.1002/9783527680870.
(7) Wang, Z.; Joshi, S.; Savel'ev, S. E.; Jiang, H.; Midya, R.; Lin, P.; Hu, M.; Ge, N.; Strachan, J. P.; Li, Z.; Wu, Q.; Barnell, M.; Li, G.-L.; Xin, H. L.; Williams, R. S.; Xia, Q.; Yang, J. J. Memristors with Diffusive Dynamics as Synaptic Emulators for Neuromorphic Computing. *Nat. Mater.* **2017**, *16* (1), 101−108.
(8) Jo, S. H.; Chang, T.; Ebong, I.; Bhadviya, B. B.; Mazumder, P.; Lu, W. Nanoscale Memristor Device as Synapse in Neuromorphic Systems. *Nano Lett.* **2010**, *10* (4), 1297−1301.
(9) Chekol, S. A.; Menzel, S.; Amad, R. W.; Waser, R.; Hoffmann-Eifert, S. Effect of the Threshold Kinetics on the Filament Relaxation Behavior of Ag-Based Diffusive Memristors. *Adv. Funct Materials* **2022**, *32* (15), 2111242.
(10) Li, C.; Xu, T.; Pan, R.; Bao, S.; Yin, K.; Shen, J.; Zhu, Y.; Hou, S.; Sun, L. Electric Field-Dependent Evolution Dynamics of Conductive Filaments in 2D Material-Based Planar Memristors. *ACS Nano* **2024**, *18* (46), 32196−32204.
(11) Sangwan, V. K.; Lee, H.-S.; Bergeron, H.; Balla, I.; Beck, M. E.; Chen, K.-S.; Hersam, M. C. Multi-Terminal Memtransistors from Polycrystalline Monolayer Molybdenum Disulfide. *Nature* **2018**, *554* (7693), 500−504.
(12) Yin, S.; Luo, Z.; Li, Q.; Xiong, C.; Liu, Y.; Singh, R.; Zeng, F.; Zhong, Y.; Zhang, X. Emulation of Learning and Memory Behaviors by Memristor Based on Ag Migration on 2D MoS_2 Surface. *Phys. Status Solidi A* **2019**, *216* (14), 1900104.
(13) Yang, Y.; Gao, P.; Gaba, S.; Chang, T.; Pan, X.; Lu, W. Observation of Conducting Filament Growth in Nanoscale Resistive Memories. *Nat. Commun.* **2012**, *3* (1), 732.
(14) Sun, L.; Zhang, Y.; Hwang, G.; Jiang, J.; Kim, D.; Eshete, Y. A.; Zhao, R.; Yang, H. Synaptic Computation Enabled by Joule Heating of Single-Layered Semiconductors for Sound Localization. *Nano Lett.* **2018**, *18* (5), 3229−3234.
(15) Nam, J. H.; Oh, S.; Jang, H. Y.; Kwon, O.; Park, H.; Park, W.; Kwon, J.; Kim, Y.; Cho, B. Low Power MoS_2 /Nb_2O_5 Memtransistor Device with Highly Reliable Heterosynaptic Plasticity. *Adv. Funct Materials* **2021**, *31* (40), 2104174.
(16) Ge, R.; Wu, X.; Kim, M.; Shi, J.; Sonde, S.; Tao, L.; Zhang, Y.; Lee, J. C.; Akinwande, D. Atomristor: Nonvolatile Resistance Switching in Atomic Sheets of Transition Metal Dichalcogenides. *Nano Lett.* **2018**, *18* (1), 434−441.
(17) Tang, B.; Veluri, H.; Li, Y.; Yu, Z. G.; Waqar, M.; Leong, J. F.; Sivan, M.; Zamburg, E.; Zhang, Y.-W.; Wang, J.; Thean, A. V.-Y. Wafer-Scale Solution-Processed 2D Material Analog Resistive Memory Array for Memory-Based Computing. *Nat. Commun.* **2022**, *13* (1), 3037.
(18) Feng, X.; Li, Y.; Wang, L.; Chen, S.; Yu, Z. G.; Tan, W. C.; Macadam, N.; Hu, G.; Huang, L.; Chen, L.; Gong, X.; Chi, D.; Hasan, T.; Thean, A. V.; Zhang, Y.; Ang, K. A Fully Printed Flexible MoS_2 Memristive Artificial Synapse with Femtojoule Switching Energy. *Adv. Elect Materials* **2019**, *5* (12), 1900740.
(19) Kim, J.; Song, J.; Kwak, H.; Choi, C.; Noh, K.; Moon, S.; Hwang, H.; Hwang, I.; Jeong, H.; Choi, S.; Kim, S.; Kim, J. K. Attojoule Hexagonal Boron Nitride-Based Memristor for High-Performance Neuromorphic Computing. *Small* **2024**, *20*, 2403737.
(20) Huh, W.; Lee, D.; Lee, C. Memristors Based on 2D Materials as an Artificial Synapse for Neuromorphic Electronics. *Adv. Mater.* **2020**, *32* (51), 2002092.
(21) Cruces, S.; Ganeriwala, M. D.; Lee, J.; Völkel, L.; Braun, D.; Grundmann, A.; Ran, K.; González Marín, E.; Kalisch, H.; Heuken, M.; Vescan, A.; Mayer, J.; Godoy, A.; Daus, A.; Lemme, M. C. Volatile MoS_2 Memristors with Lateral Silver Ion Migration for Artificial Neuron Applications. *Small Science* **2025**, *5*, 2400523.
(22) Farronato, M.; Melegari, M.; Ricci, S.; Hashemkhani, S.; Bricalli, A.; Ielmini, D. Memtransistor Devices Based on MoS_2 Multilayers with Volatile Switching Due to Ag Cation Migration. *Adv. Elect Materials* **2022**, *8* (8), 2101161.
(23) Wang, S.; Chen, C.; Yu, Z.; He, Y.; Chen, X.; Wan, Q.; Shi, Y.; Zhang, D. W.; Zhou, H.; Wang, X.; Zhou, P. A MoS_2 /PTCDA Hybrid Heterojunction Synapse with Efficient Photoelectric Dual Modulation and Versatility. *Adv. Mater.* **2019**, *31* (3), 1806227.
(24) Sangwan, V. K.; Jariwala, D.; Kim, I. S.; Chen, K.-S.; Marks, T. J.; Lauhon, L. J.; Hersam, M. C. Gate-Tunable Memristive Phenomena Mediated by Grain Boundaries in Single-Layer MoS2. *Nat. Nanotechnol.* **2015**, *10* (5), 403−406.
(25) Zhu, X.; Liang, X.; Lu, W. D. Ionic Modulation and Ionic Coupling Effects in MoS2 Devices for Neuromorphic Computing. *Nat. Mater.* **2019**, *18* (2), 141−148.
(26) Zhai, Y.; Xie, P.; Feng, Z.; Du, C.; Han, S.; Zhou, Y. 2D Heterostructure for High-Order Spatiotemporal Information Processing. *Adv. Funct Materials* **2022**, *32* (7), 2108440.
(27) Yang, Z.; Yang, Z.; Liu, L.; Li, X.; Li, J.; Xiong, C.; Mai, X.; Tong, H.; Li, Y.; Xue, K.-H.; Xue, X.; Xu, M.; Li, D.; Zhou, P.; Miao, X. Anisotropic Mass Transport Enables Distinct Synaptic Behaviors on 2D Material Surface. *Materials Today Electronics* **2023**, *5*, 100047.
(28) Zhu, J.; Yang, Y.; Jia, R.; Liang, Z.; Zhu, W.; Rehman, Z. U.; Bao, L.; Zhang, X.; Cai, Y.; Song, L.; Huang, R. Ion Gated Synaptic Transistors Based on 2D van Der Waals Crystals with Tunable Diffusive Dynamics. *Adv. Mater.* **2018**, *30* (21), 1800195.
(29) Ju, D.; Kim, S.; Park, K.; Lee, J.; Koo, M.; Kim, S. Realization of Multiple Synapse Plasticity by Coexistence of Volatile and Non-volatile Characteristics of Interface Type Memristor. *ACS Appl. Mater. Interfaces* **2024**, *16* (19), 24929−24942.
(30) Dong, Z.; Qian, L.; Li, Q.; Liu, Z.; Guo, J.; Wang, L.; Wu, S.; Xiong, R.; Liu, Y.; He, C. Coexistence of Volatile and Non-Volatile Resistive Switching Characteristics in NbOx Memristor Regulated by Electron Irradiation-Induced Surface Oxygen Vacancies. *Appl. Surf. Sci.* **2025**, *687*, 162295.
(31) Rahmani, M. K.; Yang, B.-D.; Kim, H.; Kim, H.; Kang, M. H. Coexistence of Volatile and Non-Volatile Resistive Switching in Ni/SiO_2 /Pt Memristor Device Controlled from Different Current Compliances. *Semicond. Sci. Technol.* **2021**, *36* (9), 095031.
(32) Shi, Y.; Pan, C.; Chen, V.; Raghavan, N.; Pey, K. L.; Puglisi, F. M.; Pop, E.; Wong, H.-S. P.; Lanza, M. Coexistence of Volatile and Non-Volatile Resistive Switching in 2D h-BN Based Electronic Synapses. In *2017 IEEE International Electron Devices Meeting (IEDM)*; IEEE: San Francisco, CA, USA, 2017; pp 5.4.1−5.4.4. DOI: 10.1109/IEDM.2017.8268333.
(33) Yang, S. J.; Liang, L.; Lee, Y.; Gu, Y.; Fatheema, J.; Kutagulla, S.; Kim, D.; Kim, M.; Kim, S.; Akinwande, D. Volatile and Nonvolatile Resistive Switching Coexistence in Conductive Point Hexagonal Boron Nitride Monolayer. *ACS Nano* **2024**, *18* (4), 3313−3322.
(34) Yun, S.; Park, J.; Kang, M.; Kim, S. Coexistence of Non-Volatile and Volatile Characteristics of the Pt/TaOx/TiN Device. *Results in Physics* **2022**, *34*, 105307.
(35) Wang, W.; Wang, M.; Ambrosi, E.; Bricalli, A.; Laudato, M.; Sun, Z.; Chen, X.; Ielmini, D. Surface Diffusion-Limited Lifetime of Silver and Copper Nanofilaments in Resistive Switching Devices. *Nat. Commun.* **2019**, *10* (1), 81.
(36) Rademacher, N.; Reato, E.; Völkel, L.; Grundmann, A.; Heuken, M.; Kalisch, H.; Vescan, A.; Daus, A.; Lemme, M. C. CVD Graphene-MoS2 Van Der Waals Heterostructures on the Millimeter-Scale. *Micro and Nano Engineering* **2024**, *23*, 100256.
(37) Xiao, J.; Long, M.; Li, X.; Zhang, Q.; Xu, H.; Chan, K. S. Effects of van Der Waals Interaction and Electric Field on the Electronic Structure of Bilayer MoS_2. *J. Phys.: Condens. Matter* **2014**, *26* (40), 405302.

(38) Ranganathan, K.; Fiegenbaum-Raz, M.; Ismach, A. Large-Scale and Robust Multifunctional Vertically Aligned MoS_2 Photo-Memristors. *Adv. Funct Materials* **2020**, *30* (51), 2005718.
(39) Li, H.; Zhang, Q.; Yap, C. C. R.; Tay, B. K.; Edwin, T. H. T.; Olivier, A.; Baillargeat, D. From Bulk to Monolayer MoS_2%: Evolution of Raman Scattering. *Adv. Funct Materials* **2012**, *22* (7), 1385−1390.
(40) Lee, C.; Yan, H.; Brus, L. E.; Heinz, T. F.; Hone, J.; Ryu, S. Anomalous Lattice Vibrations of Single- and Few-Layer MoS_2. *ACS Nano* **2010**, *4* (5), 2695−2700.
(41) Sarkar, S.; Mathew, S.; Chintalapati, S.; Rath, A.; Panahandeh-Fard, M.; Saha, S.; Goswami, S.; Tan, S. J. R.; Loh, K. P.; Scott, M.; Venkatesan, T. Direct Bandgap-like Strong Photoluminescence from Twisted Multilayer MoS_2 Grown on $SrTiO_3$. *ACS Nano* **2020**, *14* (12), 16761−16769.
(42) Eda, G.; Yamaguchi, H.; Voiry, D.; Fujita, T.; Chen, M.; Chhowalla, M. Photoluminescence from Chemically Exfoliated MoS_2. *Nano Lett.* **2011**, *11* (12), 5111−5116.
(43) Scheuschner, N.; Ochedowski, O.; Kaulitz, A.-M.; Gillen, R.; Schleberger, M.; Maultzsch, J. Photoluminescence of Freestanding Single- and Few-Layer MoS 2. *Phys. Rev. B* **2014**, *89* (12), 125406.
(44) Sun, Q.; Chen, G. Learning Model Based on Electrochemical Metallization Memristor with Cluster Residual Effect. *Physica Status Solidi (b)* **2024**, 2400170.
(45) Ohno, T.; Hasegawa, T.; Tsuruoka, T.; Terabe, K.; Gimzewski, J. K.; Aono, M. Short-Term Plasticity and Long-Term Potentiation Mimicked in Single Inorganic Synapses. *Nat. Mater.* **2011**, *10* (8), 591−595.
(46) Lee, G.; Baek, J.; Ren, F.; Pearton, S. J.; Lee, G.; Kim, J. Artificial Neuron and Synapse Devices Based on 2D Materials. *Small* **2021**, *17* (20), 2100640.
(47) Bousoulas, P.; Panagopoulou, M.; Boukos, N.; Tsoukalas, D. Emulating Artificial Neuron and Synaptic Properties with SiO_2 -Based Memristive Devices by Tuning Threshold and Bipolar Switching Effects. *J. Phys. D: Appl. Phys.* **2021**, *54* (22), 225303.
(48) Sze, S. M.; Li, Y.; Ng, K. K. *Physics of Semiconductor Devices*, Fourth ed..; Wiley: Hoboken, NJ, 2021.
(49) Wetzelaer, G. A. H.; Blom, P. W. M. Ohmic Current in Organic Metal-Insulator-Metal Diodes Revisited. *Phys. Rev. B* **2014**, *89* (24), 241201.
(50) Daus, A.; Jaikissoon, M.; Khan, A. I.; Kumar, A.; Grady, R. W.; Saraswat, K. C.; Pop, E. Fast-Response Flexible Temperature Sensors with Atomically Thin Molybdenum Disulfide. *Nano Lett.* **2022**, *22* (15), 6135−6140.
(51) Ashcroft, N. W.; Mermin, N. D. *Solid State Physics*; Saunders College Publishing: Fort Worth, 1976.
(52) Dev, D.; Krishnaprasad, A.; Shawkat, M. S.; He, Z.; Das, S.; Fan, D.; Chung, H.-S.; Jung, Y.; Roy, T. 2D MoS_2 -Based Threshold Switching Memristor for Artificial Neuron. *IEEE Electron Device Lett.* **2020**, *41* (6), 936−939.

https://doi.org/10.1021/acs.nanolett.5c01992
Nano Lett. 2025, 25, 12455−12462